Magnetic Field Amplification by the Weibel Instability at Planetary and Astrophysical Shocks with High Mach Number

Artem Bohdan[1,*] Martin Pohl[1,2] Jacek Niemiec[3] Paul J. Morris[1] Yosuke Matsumoto[4]
Takanobu Amano[5] Masahiro Hoshino[5] and Ali Sulaiman[6]

[1]*DESY, DE-15738 Zeuthen, Germany*
[2]*Institute of Physics and Astronomy, University of Potsdam, DE-14476 Potsdam, Germany*
[3]*Institute of Nuclear Physics Polish Academy of Sciences, PL-31342 Krakow, Poland*
[4]*Department of Physics, Chiba University, 1-33 Yayoi-cho, Inage-ku, Chiba 263-8522, Japan*
[5]*Department of Earth and Planetary Science, University of Tokyo, 7-3-1 Hongo, Bunkyo-ku, Tokyo 113-0033, Japan*
[6]*Department of Physics and Astronomy, University of Iowa, Iowa City, Iowa 52242, USA*

Collisionless shocks are ubiquitous in the Universe and often associated with a strong magnetic field. Here, we use large-scale particle-in-cell simulations of nonrelativistic perpendicular shocks in the high-Mach-number regime to study the amplification of the magnetic field within shocks. The magnetic field is amplified at the shock transition due to the ion-ion two-stream Weibel instability. The normalized magnetic field strength strongly correlates with the Alfvénic Mach number. Mock spacecraft measurements derived from particle-in-cell simulations are fully consistent with those taken *in situ* at Saturn's bow shock by the Cassini spacecraft.

Collisionless shocks are ubiquitous in the Universe, and they are observed in planetary systems, supernova remnants (SNRs), jets of active galactic nuclei, galaxy clusters, etc. In contrast to fluid shock waves, where dissipation at the shock front is mediated by binary collisions, collisionless shocks are shaped by collective particle interactions with interaction lengths much shorter than the collisional mean free path [1,2]. Collisionless shocks are usually magnetized, and magnetic fields play a key role in their physics. The jump condition for the magnetic field [3] and the internal shock structure [4] strongly depends on the shock obliquity. magnetic field turbulence near the shock is a key ingredient of diffusive shock acceleration (DSA) [5–10] and shapes nonthermal x-ray emission. Amplified magnetic fields (at scales much larger than the upstream ion gyroradius) have been inferred from observations of SNRs through the detection of nonthermal x-ray rims [11–14], fast temporal variability of x-ray hot spots [15], and the γ-ray/x-ray flux ratio [16]. We know various possible mechanisms for magnetic field amplification at these scales: cosmic-ray-driven nonresonant modes [17,18], fluid vorticity downstream of the shock seeded by upstream density inhomogeneities [19,20], cosmic-ray pressure-driven magnetic field amplification [21,22], and inverse cascading of relatively short-scale Alfvén waves [23].

Here, we study magnetic field amplification on scales smaller than the upstream ion gyroradius at high-Mach-number quasiperpendicular shocks. *In situ* measurements by the Cassini spacecraft [24,25] reveal the detailed magnetic field structure of Saturn's bow shock with resolution below the ion gyroradius. The Alfvénic Mach number of this shock can reach values of around 200, which is similar to that of SNR shocks. Reference [25] demonstrated that the normalized overshoot magnetic field strength displays a strong positive correlation with M_A across the entire range of measured M_A. Particularly strong amplification is observed at shocks at which shock self-reformation is evident [24]. Reasons for such behavior are unknown, and they are the objective of our study.

Leroy's calculations [26] for perpendicular shocks combined with hybrid simulations suggest that the overshoot magnetic field strength (B_{over}) can be estimated as

$$B_{\text{over}} \approx 0.4 B_0 M_A^{7/6},\qquad(1)$$

where B_0 is the upstream field strength. The prefactor of 0.4 was determined with simulations [27,28]. In this model, the magnetic field amplification is associated only with plasma compression, and multidimensional effects may not be accounted for. However, three-dimensional (3D) [29], and some two-dimensional (2D) [30,31], particle-in-cell (PIC) simulations of quasiperpendicular high-M_A shocks demonstrate strong amplification of the upstream magnetic field due to the ion-ion filamentation/Weibel instability [32,33], which results from the interaction of upstream and shock-reflected ions. The mediation of high-M_A shocks by the Weibel instability is also confirmed by laboratory experiments [34] and *in situ* measurements of the Earth's bow shock at $M_A \simeq 39$ [35]. In this Letter, we discuss a mechanism of magnetic

field amplification that is based on a realistic description of perpendicular nonrelativistic high-M_A shocks and can explain the correlation between field strength and M_A observed with Cassini at Saturn's bow shock.

To tackle this issue, we use 2D PIC simulations with an *in-plane* magnetic field configuration, which permits a good approximation of realistic 3D shocks [29,36]. We perform shock simulations using an optimized fully relativistic electromagnetic 2D code with message passing interface parallelization developed from tridimensional stanford code [37–39]. Shocks are initialized with a modified flow-flow method [40]. The collision of two counterstreaming electron-ion plasma flows, each described with 20 particles per cell per species, spawns two independent shocks propagating in opposite directions. The inflow speed of two beams is $v_L = v_R = v_0 = 0.2c$. The plasma temperature for two flows differs by a factor of 1000; therefore, *electron* plasma betas (the ratio of the electron plasma pressure to the magnetic pressure) are 5×10^{-4} and 0.5 for the *left* (runs *1) and the *right* (runs *2) shocks, respectively.

The large-scale magnetic field, $\mathbf{B_0}$, is perpendicular to the shock normal ($\theta_{Bn} = 90°$) and lies in the simulation plane (the in-plane configuration, $\varphi = 0°$). The adiabatic index is $\Gamma_{ad} = \frac{5}{3}$, the shock compression ratio is about four, and the shock speed in the *upstream* frame is $v_{sh} = 0.263c$. The Alfvén velocity is $v_A = B_0/\sqrt{\mu_0(N_e m_e + N_i m_i)}$, where μ_0 is the vacuum permeability; and N_i and N_e are the ion and electron number densities. The sound speed reads $c_s = (\Gamma_{ad}k_B T_i/m_i)^{1/2}$, where k_B is the Boltzmann constant and T_i is the ion temperature. The Alfvénic ($M_A = v_{sh}/v_A$) and sonic ($M_s = v_{sh}/c_s$) Mach numbers of the shocks are defined in the conventional upstream frame (Table I).

TABLE I. Parameters of simulation runs. Listed are the ion-to-electron mass ratio, m_i/m_e; the Alfvénic and sonic Mach numbers, M_A and M_s; and the electron plasma beta β_e. Some values are shown separately for left (runs *1) and right (runs *2) shocks. Results for runs marked by a dagger (†) are not discussed in this Letter because of strong numerical noise at shock upstream. All runs use the in-plane magnetic field configuration, $\varphi = 0°$.

Runs	m_i/m_e	M_A	M_s *1	M_s *2	β_e *1	β_e *2
A1, A2	50	22.6	1104	35	5×10^{-4}	0.5
B1, B2	100	31.8	1550	49	5×10^{-4}	0.5
C1, C2	100	46	2242	71	5×10^{-4}	0.5
D1, D2	200	32	1550	49	5×10^{-4}	0.5
E1, E2	200	44.9	2191	69	5×10^{-4}	0.5
F1, F2	400	68.7	3353	106	5×10^{-4}	0.5
G1, G2	50	68.7	3353	106	5×10^{-4}	0.5
H1†, H2	50	100	4870	154	5×10^{-4}	0.5
I1†, I2	50	150	7336	232	5×10^{-4}	0.5

The ratio of the electron plasma frequency ($\omega_{pe} = \sqrt{e^2 N_e/\epsilon_0 m_e}$) to the electron gyrofrequency ($\Omega_e = eB_0/m_e$) is in the range $\omega_{pe}/\Omega_e = 8.5-80$. Here, e is the electron charge, and ϵ_0 is the vacuum permittivity. The temporal and spatial resolutions are $\delta t = (1/40)\omega_{pe}^{-1}$ and $\Delta = (1/20)\lambda_{se}$, where λ_{se} is the electron skin depth. The transverse box size is $L_y = (8 - 24)\lambda_{si}$, where $\lambda_{si} = \sqrt{m_i/m_e}\lambda_{se}$ is the ion skin depth. The simulation time is about $T \approx 8\Omega_i^{-1}$, where $\Omega_i = eB_0/m_i$.

Our simulations cover a wide range of physical parameters: $M_A = 22.6-150$, $m_i/m_e = 50-400$, and $\beta_{e,R} = 5 \times 10^{-4} - 0.5$. Hence, we can compare our simulation results with data for Saturn's bow shock for $M_A \geq 20$.

Figure 1(a) shows an electron-density map of the fully developed shock from run B2. The shock position, x_{sh}, is defined as the position of the shock overshoot. Buneman waves are visible as small-scale density ripples at $x - x_{sh} \approx (8 - 12)\lambda_{si}$. The Weibel instability is represented by density filaments at $x - x_{sh} \approx (2 - 10)\lambda_{si}$. The downstream region is at $x - x_{sh} < -5\lambda_{si}$. This structure is representative for all runs and for the high-M_A regime in general [30,31,36,41–44]. Earlier linear analysis [30] and its adaptation to our study [43] both indicate that high-M_A shocks are Weibel-instability mediated.

Figure 1(b) displays the density and magnetic field profiles at the shock transition of run B2, averaged in time over two cycles of shock reformation. The plasma compression reaches $N_{over}/N_0 \approx 7$ at the shock overshoot in all simulations, which is not in line with Leroy's model, where
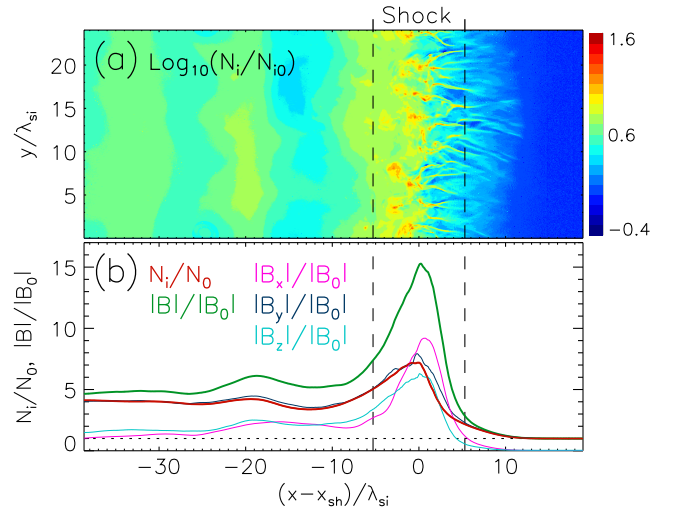

FIG. 1. Density and magnetic field in run B2: (a) ion density in logarithmic units; and (b) profile of normalized ion density (red line), profile of normalized magnetic field (green line), B_x/B_0 (magenta line), B_y/B_0 (dark blue line), and B_z/B_0 (light blue line). Profiles are calculated in the shock reference frame and averaged over the shock reformation cycle. The shock region is marked by dashed lines, and x_{sh} is the shock position.

N_{over} depends on M_A. The field strength increases twice as much, indicating substantial noncompressional magnetic field amplification.

The B_y profile almost coincides with that expected for simple compression of B_y according to the density profile. The modest increase of B_y around $(x - x_{\text{sh}})/\lambda_{\text{si}} \approx (0-3)$ is due to magnetic reconnection, which turns B_x into B_y when magnetic loops elongated in the x direction break up into chains of magnetic vortices [43]. As expected, B_x and B_z grow due to folding of the magnetic field by the Weibel modes whose wave vector is perpendicular to the relative velocity of shock-reflected and incoming upstream ions [30,31]. Further straightening of magnetic field lines leads to convergence of the density and magnetic field profiles at the shock downstream.

We define the shock region as a sector of width $L_{\text{sh}} = r_{\text{gi,up}}/3$ centered at x_{sh}, where $r_{\text{gi,up}} = M_A \lambda_{\text{si}}$. The numerical coefficient is chosen to match the shock width and the average ion gyroradius at the shock transition layer; its exact value has little, if any, impact on the results discussed here. The shock region for run B2 is marked with dashed lines in Fig. 1.

In Fig. 2, we present the amplitude [Fig. 2(a)] and energy density [Fig. 2(b)] of the magnetic field in the shock region, averaged over the shock self-reformation cycle and with error bars reflecting the level of temporal variation. The normalized field strength, $|B_{\text{sh}}|/B_0$, grows with increasing M_A. The Weibel growth rate is about $\Gamma \approx 0.1\omega_{\text{pi}}$, regardless of the shock parameters [43]. Shock self-reformation limits

the time available for the Weibel instability to develop to about Ω_i^{-1}, implying that the number of exponential growth cycles is proportional to M_A for a given shock speed. Exponential growth of the amplitude of Weibel filaments is not observed though, even at low M_A. In fact, the Weibel instability quickly becomes nonlinear, and the magnetic field strength defies an analytical derivation. Here, we can only estimate it as [green line in Fig. 2(a)]

$$|B_{\text{sh}}| \approx 2\sqrt{M_A} B_0. \qquad (2)$$

The normalized energy density of the magnetic field can be expressed as

$$\frac{U_{\text{sh,B}}}{U_{\text{sh,i}}} = \frac{B^2}{\mu_0 N_i m_i v_{\text{sh}}^2} \approx \frac{4}{M_A}, \qquad (3)$$

which is a descending trend [green line in Fig. 2(b)] that well reproduces the energy density observed in the simulations. A lower limit for the normalized magnetic energy density should be provided at very high M_A or unmagnetized shocks. For the latter, the fraction of magnetic energy in the shock region is about $U_B = 0.006U_{\text{sh,i}}$ [45], which with Eq. (3) is expected at $M_A \approx 670$, where $|B_{\text{sh}}| \approx 50B_0$.

The magnetic field remains amplified for only a few ion gyroradii behind the shock; and far downstream, the field strength is $4B_0$. Our simulation time is too short to fully capture the entire relaxation, especially for high M_A. The data we have suggest that the length scale of relaxation is roughly proportional to $|B_{\text{sh}}|/|B_0|$.

We use the analytical description presented in [43] to clarify the relation between the Weibel growth rate and the choice of plasma parameters, namely, the upstream plasma beta, the mass ratio, and the shock speed. Runs *1 and *2 differ by the upstream plasma temperature. At the shock foot, however, the temperature of the plasma constituents is similar on account of partial thermalization, which leads to similar Weibel growth rates. Runs that differ only in the mass ratio also show the same magnetic field amplification level. We use the plasma parameters observed in the shock foot of run F2 to calculate the Weibel-instability growth rate for different mass ratios, keeping all kinetic and thermal parameters constant. We find that the growth rate of the most unstable mode remains the same within an ∼10% margin [Fig. 3(a)]. Therefore, we conclude that the upstream plasma beta and the mass ratio do not play a significant role in magnetic field amplification.

We also explore how the behavior of the Weibel instability depends on the shock speed, which in the simulations is two orders of magnitude higher than at Saturn's bow shock. Figure 3(b) shows the Weibel-instability growth rates for three values of the shock velocity: $0.26c$, $0.026c$, and $0.0026c$. The last case with $v_{\text{sh}} = 780$ km/s is very close to the speed of Saturn's bow shock, which is about 400 km/s [46]. For $v_{\text{sh}} = 0.26c$, we
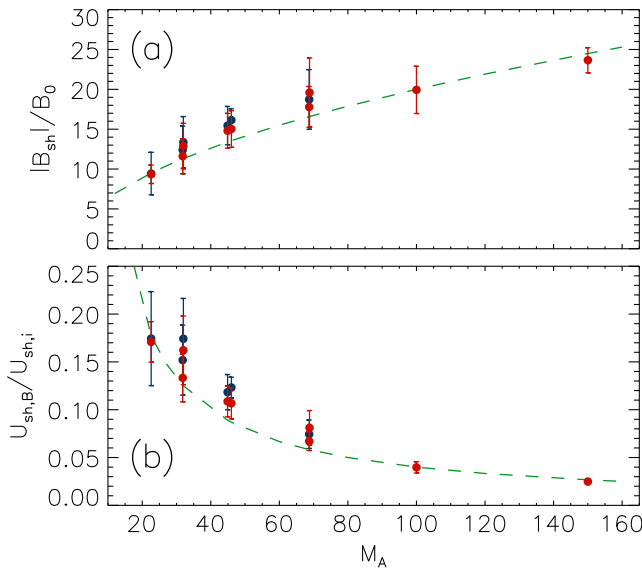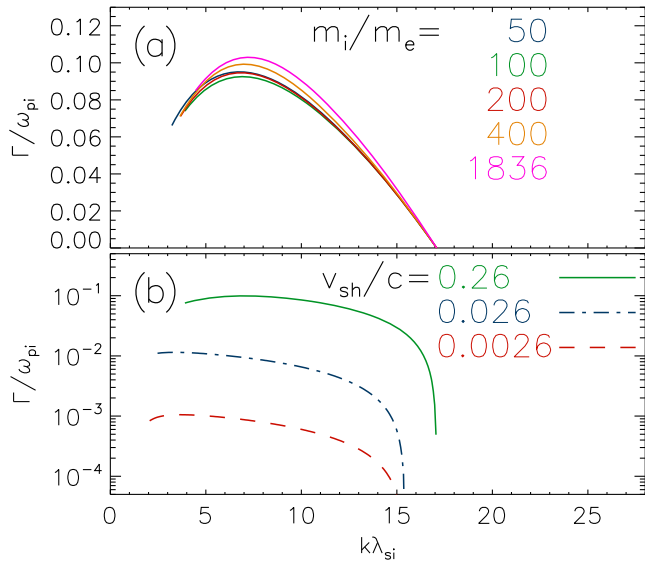

FIG. 2. Normalized magnetic field strength (a) and magnetic energy density normalized by upstream ion energy density (b), both evaluated in the shock region defined in Fig. 1. Blue and red colors correspond to left ($\beta = 5 \times 10^{-4}$) and right ($\beta = 0.5$) shocks, respectively. The green dotted line in Fig. 2(a) reflects $|B_{\text{sh}}|/B_0 = 2\sqrt{M_A}$, and that in Fig. 2(b) shows $U_{\text{sh,B}}/U_{\text{sh,i}} = 4M_A^{-1}$.

FIG. 3. Growth rate of Weibel modes for five mass ratios (a) and three shock speeds (b).
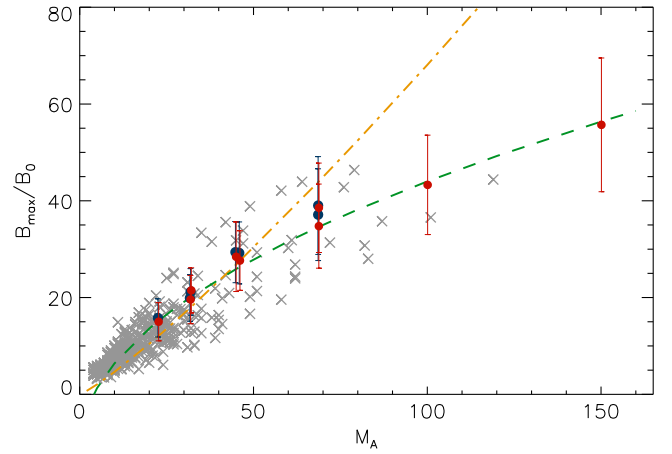

FIG. 4. Cassini measurements [25] indicated by gray crosses and PIC simulation data displayed with blue and red dots for left ($\beta = 5 \times 10^{-4}$) and right ($\beta = 0.5$) shocks, respectively. The yellow dash-dotted line is an earlier prediction, $B_{\text{over}}/B_0 \approx 0.4 M_A^{7/6}/1.26$ [cf. Eq. (1)], corrected for shock reformation. The green dashed line is the behavior found in our PIC simulations, $B_{\text{max}}/B_0 = 5.5(\sqrt{M_A} - 2)$.

use plasma parameters from run F2. For the two other cases, we accordingly rescale the velocity and the temperature of the plasma flow. To be noted from Fig. 3(b) is that the normalized peak growth rate is proportional to the shock speed:

$$\Gamma_{\text{max}} \propto v_{\text{sh}} \omega_{\text{pi}} \quad \text{or} \quad \Gamma_{\text{max}} \propto M_A \Omega_i \qquad (4)$$

This finding matches the result of earlier, simplified calculations [4]. Equation (4) shows that the number of exponential growth cycles available for Weibel modes scales inversely with the Mach number, whatever the shock speed. Therefore, M_A is the only upstream parameter that defines magnetic field amplification at the shock transition.

The intrinsic shock dynamics also affects the magnetic field amplification level. Reference [24] showed that 16 shocks out of 54 shock crossings undergo shock reformation, and the measured B_{max}/B_0 (B_{max} is the maximal magnetic field measured during a shock crossing by the spacecraft) at these shocks is 1.42 times that at the other 38 shocks. This behavior is likely explained by the differences in ion reflection at the shock ramp between reforming and nonreforming shocks. With shock self-reformation, the ion reflection rate is time dependent and swings periodically [40], reaching larger values than for a nonreforming shock where the ion reflection rate is steady. This results in a stronger magnetic field amplification in reforming shocks, on account of the higher growth rate of Weibel modes and stronger plasma compression at the shock ramp. Therefore, B_{max}/B_0 is higher for shocks at which shock reformation is observed. In all of our simulations, shock reformation is clearly visible. To properly compare with the full set of *in situ* measurements, which includes both reforming and nonreforming shocks, we therefore reduce the peak field

strength measured in the simulations by a factor of $1.42/[1.42 n_r + (1 - n_r)] = 1.26$, where $n_r = 16/54$ is the fraction of reforming shocks in the *in situ* data of [24].

The largest set of magnetic field measurements at Saturn's bow shock [25] contains 422 shock crossings during which the shock was quasiperpendicular ($\theta_{B_n} \geq 45°$) and for which B_{max}/B_0 is indicated by gray crosses in Fig. 4. We derive B_{max}/B_0 from PIC simulation data, assuming that a virtual spacecraft crosses a simulated shock with a straight trajectory. On the spacecrafts trajectory, we calculate B_{max}/B_0; and then we average it over all possible shock crossing points and the speed and flight direction of the virtual spacecraft. Hereby, we account for both the temporal and the spatial variations of B_{max}/B_0. The results are shown in Fig. 4 as blue and red dots with error bars. Note that we already applied, to both our results and Leroy's model, the downward correction by a factor of 1.26, which we discussed in the preceding paragraph as compensation for shock reformation.

Figure 4 demonstrates a good match between the *in situ* measurement and simulation data. A good fit of the simulation data is shown as a green dashed line in Fig. 4,

$$\frac{B_{\text{max}}}{B_0} = 5.5(\sqrt{M_A} - 2), \qquad (5)$$

which also well describes the *in situ* measurements for $M_A \gtrsim 10$. This is not proof that magnetic fields are defined by Weibel instability at $10 < M_A < 20$, but at least Eq. (5) can be used to estimate the field strength. For comparison, the yellow dash-dotted line in Fig. 4 shows the scaling of Eq. (1), which also was confirmed with recent 2D simulations [28]. However, 2D simulations cannot always

capture realistic shock physics and the *out-of-plane* magnetic field configuration utilized in [28] misses the Weibel instability, which changes the magnetic field amplification physics compared to our in-plane 2D simulations and the 3D simulations of [29]. Although Eq. (1) matches the data reasonably well for $M_A < 60$, even that may be a coincidence because this model relies on simplified one-dimensional shock physics. In our view, Eq. (5) is a better and physically motivated approximation for B_{max}/B_0 at shocks with $M_A \gtrsim 10$.

In addition to the previous result, good fit of B_{max}/B_0, the shock reformation period, $T_{reform} \approx 1.5 \, \Omega_i^{-1}$, is the same in our simulations and in the Cassini data [24]. Also, the magnetic field relaxation distance is similar with about one shock width, further suggesting similar physical processes at play in PIC simulations and real bow shocks.

We find no evidence for magnetic field amplification by ion beam cyclotron instabilities. They would require more time to develop ($T \gg \Omega_i^{-1}$), and usually these instabilities are observed at quasiparallel shocks where the shock-reflected ions can move far upstream.

We have established a strong connection between the Weibel instability and magnetic field amplification at high-M_A shocks. The results of our PIC simulations are fully consistent with *in situ* measurements of Saturn's bow shock. As M_A is the only relevant parameter, our findings on field amplification inside the shock transition layer should also apply to SNR shocks. Weibel modes can increase the local synchrotron emissivity by a factor of $(B_{sh}/B_0)^2$, which may reach 1000. Larger enhancements arise in the x-ray band beyond the synchrotron peak frequency; but overall, the effect is likely unobservable with current facilities due to low resolution. However, the interaction of Weibel modes with other amplification processes may introduce significant changes in the shock structure, and it should be taken into account in further studies.

Electron preacceleration [36,43] and heating [44] strongly depend on the structure and strength of the magnetic field. At quasiperpendicular shocks, where stochastic shock drift acceleration (SSDA) is expected to operate [29,47], a strong magnetic field generated by the Weibel instability limits the mean free path and increases the cyclotron frequency of electrons, and so the cutoff energy of SSDA may depend on M_A.

Also, due to the strong magnetic field at the shock transition, particles require larger momenta for injection into classical DSA; they repeatedly cross the shock without significant deflection in the shock internal structure. The Larmor radius in the amplified field [Eq. (2)] should then be much larger than the shock width, $r_{sh} \propto r_{gi,up} \propto B_0^{-1}$, which implies for the injection momentum

$$p_{inj} \propto r_{sh} B_{sh} \propto \sqrt{M_A}, \qquad (6)$$

at Weibel-mediated shocks.

---

*artem.bohdan@desy.de

[1] R. Z. Sagdeev, Cooperative phenomena and shock waves in collisionless plasmas, Rev. Plasma Phys. **4**, 23 (1966), https://ui.adsabs.harvard.edu/abs/1966RvPP....4...23S.

[2] D. A. Tidman and N. A. Krall, *Shock Waves in Collisionless Plasmas* (Wiley Series in Plasma Physics, New York, 1971), https://ui.adsabs.harvard.edu/abs/1971swcp.book.....T.

[3] A. Bret, Can we trust MHD jump conditions for collisionless shocks?, Astrophys. J. **900**, 111 (2020).

[4] R. A. Treumann, Fundamentals of collisionless shocks for astrophysical application, 1. Non-relativistic shocks, Astron. Astrophys. Rev. **17**, 409 (2009).

[5] W. I. Axford, E. Leer, and G. Skadron, The acceleration of cosmic rays by shock waves, in *15th International Cosmic Ray Conference, Budapest, 1977* (Bulgarska akademiia na naukite, 1977), p. 132, https://ui.adsabs.harvard.edu/abs/1977ICRC...11..132A/abstract.

[6] G. F. Krymskii, A regular mechanism for the acceleration of charged particles on the front of a shock wave, Dokl. Akad. Nauk SSSR **234**, 1306 (1977), https://ui.adsabs.harvard.edu/abs/1977DoSSR.234.1306K.

[7] L. O. Drury, Review article: An introduction to the theory of diffusive shock acceleration of energetic particles in tenuous plasmas, Rep. Prog. Phys. **46**, 973 (1983).

[8] A. R. Bell, The acceleration of cosmic rays in shock fronts. I, Mon. Not. R. Astron. Soc. **182**, 147 (1978).

[9] A. R. Bell, The acceleration of cosmic rays in shock fronts. II, Mon. Not. R. Astron. Soc. **182**, 443 (1978).

[10] R. D. Blandford and J. P. Ostriker, Particle acceleration by astrophysical shocks, Astrophys. J. Lett. **221**, L29 (1978).

[11] J. Vink and J. M. Laming, On the magnetic fields and particle acceleration in Cassiopeia A, Astrophys. J. **584**, 758 (2003).

[12] A. Bamba, R. Yamazaki, M. Ueno, and K. Koyama, Fine structure of the thermal and non-thermal x-rays in the SN 1006 shell, Adv. Space Res. **33**, 376 (2004).

[13] M. Pohl, H. Yan, and A. Lazarian, Magnetically limited x-ray filaments in young supernova remnants, Astrophys. J. Lett. **626**, L101 (2005).

[14] J. Vink, Supernova remnants: the x-ray perspective, Astron. Astrophys. Rev. **20**, 49 (2012).

[15] Y. Uchiyama, F. A. Aharonian, T. Tanaka, T. Takahashi, and Y. Maeda, Extremely fast acceleration of cosmic rays in a supernova remnant, Nature (London) **449**, 576 (2007).

[16] V. A. Acciari *et al.*, Discovery of TeV gamma-ray emission from Tycho's supernova remnant, Astrophys. J. Lett. **730**, L20 (2011).

[17] A. R. Bell, Turbulent amplification of magnetic field and diffusive shock acceleration of cosmic rays, Mon. Not. R. Astron. Soc. **353,** 550 (2004).

[18] A. R. Bell, The interaction of cosmic rays and magnetized plasma, Mon. Not. R. Astron. Soc. **358,** 181 (2005).

[19] J. Giacalone and J. R. Jokipii, Magnetic field amplification by shocks in turbulent fluids, Astrophys. J. Lett. **663,** L41 (2007).

[20] F. Fraschetti, Turbulent amplification of a magnetic field driven by the dynamo effect at rippled shocks, Astrophys. J. **770,** 84 (2013).

[21] T. P. Downes, Driven multifluid magnetohydrodynamic molecular cloud turbulence, Mon. Not. R. Astron. Soc. **425,** 2277 (2012).

[22] T. P. Downes and L. O. Drury, Cosmic ray pressure driven magnetic field amplification: Dimensional, radiative and field orientation effects, Mon. Not. R. Astron. Soc. **444,** 365 (2014).

[23] P. H. Diamond and M. A. Malkov, Dynamics of mesoscale magnetic field in diffusive shock acceleration, Astrophys. J. **654,** 252 (2007).

[24] A. H. Sulaiman, A. Masters, M. K. Dougherty, D. Burgess, M. Fujimoto, and G. B. Hospodarsky, Quasiperpendicular High Mach Number Shocks, Phys. Rev. Lett. **115,** 125001 (2015).

[25] A. H. Sulaiman, A. Masters, and M. K. Dougherty, Characterization of Saturn's bow shock: Magnetic field observations of quasi-perpendicular shocks, J. Geophys. Res.: Space Phys. **121,** 4425 (2016).

[26] M. M. Leroy, Structure of perpendicular shocks in collisionless plasma, Phys. Fluids **26,** 2742 (1983).

[27] K. B. Quest, Simulations of high Mach number perpendicular shocks with resistive electrons, J. Geophys. Res. **91,** 8805 (1986).

[28] Y. Matsumoto, T. Amano, and M. Hoshino, Electron accelerations at high mach number shocks: Two-dimensional particle-in-cell simulations in various parameter regimes, Astrophys. J. **755,** 109 (2012).

[29] Y. Matsumoto, T. Amano, T. N. Kato, and M. Hoshino, Electron Surfing and Drift Accelerations in a Weibel-Dominated High-Mach-Number Shock, Phys. Rev. Lett. **119,** 105101 (2017).

[30] T. N. Kato and H. Takabe, Nonrelativistic collisionless shocks in weakly magnetized electron-ion plasmas: Two-dimensional particle-in-cell simulation of perpendicular shock, Astrophys. J. **721,** 828 (2010).

[31] Y. Matsumoto, T. Amano, T. N. Kato, and M. Hoshino, Stochastic electron acceleration during spontaneous turbulent reconnection in a strong shock wave, Science **347,** 974 (2015).

[32] E. S. Weibel, Spontaneously Growing Transverse Waves in a Plasma Due to an Anisotropic Velocity Distribution, Phys. Rev. Lett. **2,** 83 (1959).

[33] B. D. Fried, Mechanism for instability of transverse plasma waves, Phys. Fluids **2,** 337 (1959).

[34] F. Fiuza, G. F. Swadling, A. Grassi, H. G. Rinderknecht, D. P. Higginson, D. D. Ryutov, C. Bruulsema, R. P. Drake, S. Funk, S. Glenzer, G. Gregori, C. K. Li, B. B. Pollock, B. A. Remington, J. S. Ross, W. Rozmus, Y. Sakawa, A. Spitkovsky, S. Wilks, and H. S. Park, Electron acceleration in laboratory-produced turbulent collisionless shocks, Nat. Phys. **16,** 916 (2020).

[35] T. Sundberg, D. Burgess, M. Scholer, A. Masters, and A. H. Sulaiman, The dynamics of very high Alfvén Mach number shocks in space plasmas, Astrophys. J. **836,** L4 (2017).

[36] A. Bohdan, J. Niemiec, O. Kobzar, and M. Pohl, Electron pre-acceleration at nonrelativistic high-Mach-number perpendicular shocks, Astrophys. J. **847,** 71 (2017).

[37] O. Buneman, TRISTAN: The 3-d electromagnetic particle code, *Computer Space Plasma Physics: Simulation Techniques and Software*, edited by H. Matsumoto and Y. Omura (Terra Scientific, Tokyo, 1993), p. 67.

[38] J. Niemiec, M. Pohl, T. Stroman, and K.-I. Nishikawa, Production of magnetic turbulence by cosmic rays drifting upstream of supernova remnant shocks, Astrophys. J. **684,** 1174 (2008).

[39] A. Dorobisz, M. Kotwica, J. Niemiec, O. Kobzar, A. Bohdan, and K. Wiatr, The impact of particle sorting on particle-in-cell simulation performance, in *Parallel Processing and Applied Mathematics*, edited by R. Wyrzykowski, J. Dongarra, E. Deelman, and K. Karczewski (Springer International, Cham, 2018), p. 156.

[40] V. Wieland, M. Pohl, J. Niemiec, I. Rafighi, and K.-I. Nishikawa, Nonrelativistic perpendicular shocks modeling young supernova remnants: Nonstationary dynamics and particle acceleration at forward and reverse shocks, Astrophys. J. **820,** 62 (2016).

[41] A. Bohdan, J. Niemiec, M. Pohl, Y. Matsumoto, T. Amano, and M. Hoshino, Kinetic simulations of nonrelativistic perpendicular shocks of young supernova remnants. I. Electron shock-surfing acceleration, Astrophys. J. **878,** 5 (2019).

[42] A. Bohdan, J. Niemiec, M. Pohl, Y. Matsumoto, T. Amano, and M. Hoshino, Kinetic simulations of nonrelativistic perpendicular shocks of young supernova remnants. II. Influence of shock-surfing acceleration on downstream electron spectra, Astrophys. J. **885,** 10 (2019).

[43] A. Bohdan, M. Pohl, J. Niemiec, S. Vafin, Y. Matsumoto, T. Amano, and M. Hoshino, Kinetic simulations of nonrelativistic perpendicular shocks of young supernova remnants. III. Magnetic reconnection, Astrophys. J. **893,** 6 (2020).

[44] A. Bohdan, M. Pohl, J. Niemiec, P. Morris, Y. Matsumoto, T. Amano, and M. Hoshino, Kinetic simulation of nonrelativistic perpendicular shocks of young supernova remnants. IV. Electron heating, Astrophys. J. **904,** 12 (2020).

[45] T. N. Kato and H. Takabe, Nonrelativistic collisionless shocks in unmagnetized electron-ion plasmas, Astrophys. J. Lett. **681,** L93 (2008).

[46] N. Achilleos, C. Bertucci, C. T. Russell, G. B. Hospodarsky, A. M. Rymer, C. S. Arridge, M. E. Burton, M. K. Dougherty, S. Hendricks, E. J. Smith, and B. T. Tsurutani, Orientation, location, and velocity of Saturn's bow shock: Initial results from the Cassini spacecraft, J. Geophys. Res.: Space Phys. **111,** A03201 (2006).

[47] T. Katou and T. Amano, Theory of stochastic shock drift acceleration for electrons in the shock transition region, Astrophys. J. **874,** 119 (2019).